J Mater Sci (2007) 42:3454–3464
DOI 10.1007/s10853-006-0829-6

Preparation and characterization of cerium oxide templated from activated carbon

Mark Crocker · Uschi M. Graham · Rolando Gonzalez · Gary Jacobs · Erin Morris · Aurora M. Rubel · Rodney Andrews

Received: 10 January 2006 / Accepted: 21 August 2006 / Published online: 20 January 2007

Abstract The application of carbon templating to the preparation of cerium oxide and cerium–zirconium mixed oxide was investigated. Impregnation of a highly mesoporous activated carbon (Darco KB-B) with aqueous cerium nitrate, followed by calcination to remove the template, afforded nanocrystalline ceria with a surface area of up to 148 m^2/g. Ceria-zirconia with surface area of 148 m^2/g was similarly prepared. TEM studies on the ceria product revealed the presence of a polycrystalline phase, comprised of irregular aggregates of ceria crystallites of ca. 6.5 nm diameter. Use of activated carbon fibers (ACFs) as templates afforded ceria with a gross morphology resembling that of the fiber template. The lower surface areas (3–59 m^2/g) of the resulting ceria reflect the mainly microporous nature of the ACFs; evidently the Ce nitrate solution is largely unable to penetrate the micropores. TEM showed the ceria fibers to be comprised of crystallites possessing a morphology similar to the Darco KB-B templated ceria.

Introduction

Due to its unique properties, including its ability to reversibly store oxygen, readily accessible redox couple and acido-basic surface characteristics, cerium oxide finds wide application in catalysis. Chemical processes in which ceria is employed as a catalyst or catalyst promoter include the elimination of pollutants from auto-exhaust gases using three-way catalysts, fluid catalytic cracking in refineries, and the dehydrogenation of ethylbenzene to styrene [1–3]. Ceria also shows promise as a catalyst component for low temperature water-gas shift applications [4], the preferential oxidation of CO in hydrogen-rich atmospheres (PROX) [5], and NO_x storage catalysts (also referred to as lean NO_x traps) [6]. Further, doped ceria is attracting interest for use in solid oxide fuel cells due to its high ionic conductivity [7]. In these various applications, the performance of the ceria is strongly dependent on its crystallinity and textural properties, including surface area and porosity. For example, recent studies show that for Pt/ceria water-gas shift catalysts, the rate of hydrogen formation is proportional to the surface area of the ceria support, for a given Pt loading [8].

Methods which have been employed for the preparation of high surface area ceria include precipitation [9, 10], reverse microemulsion synthesis [11], thermal decomposition of appropriate precursors (such as citrate complexes [12]), hydrazine reduction [13], sol–gel synthesis [12, 14], and hydrothermal synthesis in the presence of a surfactant [15]. Reported surface areas for the ceria products range from ca. 60 m^2/g for the citrate method, up to ~200 m^2/g for materials prepared using reverse microemulsion and hydrothermal synthesis methods. Additionally, ceria gels with high surface area and high porosity have been obtained from the hydrolysis of Ce-methoxyethanol in excess methoxyethanol [16], and from the reaction of Ce(III) salts with epoxide-based proton scavengers [17].

M. Crocker (✉) · U. M. Graham · R. Gonzalez · G. Jacobs · E. Morris · A. M. Rubel · R. Andrews
University of Kentucky Center for Applied Energy Research, 2540 Research Park Drive, Lexington, KY 40511, USA
e-mail: crocker@caer.uky.edu

Appropriate processing of these gels enabled the isolation of aerogels with surface areas of respectively 349 and 225 m^2/g after drying, albeit these values decrease significantly upon calcination of the solids to remove organic residues.

Recently, templating methods have received much attention for the preparation of porous metal oxides. In a templated synthesis, the voids of a porous template are filled with a solution or liquid precursor of a desired composition. After drying (or solidification), removal of the template affords an inverse (or negative) replica. Silica and carbon are the most widely used template materials [18, 19], although other porous materials which have been successfully used include cellulose, agarose and starches [20, 21]. Carbon-based templates are particularly attractive, due to their high surface area and porosity, coupled with the ease of template removal by combustion. This approach has been successfully used for the synthesis of a number of high surface area metal and mixed metal oxides, using amorphous activated carbon [20, 22–24], activated carbon fibers [24–26], carbon areogels [27] or mesoporous spheres [28–30] as the template. The preparation of metal oxide nanorods and nanotubes from carbon nanotubes has also been described [31, 32]. However, the preparation of high surface ceria using carbon templating does not appear to have been studied to date. This fact, coupled with a desire to prepare high surface area ceria for use in water-gas shift catalysts, prompted us to study the preparation of ceria using carbon templating. Part of this work has been communicated previously [33].

Experimental procedures

Preparation of activated carbon fibers and templated ceria

Activated carbon fibers were prepared by thermal activation of P-400 Anshan fibers (BET surface area of 60.5 m^2/g as received) under a flow of steam/N_2 at 800–900 °C for periods of between 1 and 3 h (see Table 1). Darco KB-B activated carbon was obtained from Aldrich Chemical Co. and was dried in a vacuum oven (80 °C) before use. Ceria preparation was based on the method of Schüth et al. [22]: the carbon template was gently stirred with a 3.5 M aqueous solution of cerium nitrate (Alfa Aesar, 99.5%) for 1 h, using a twofold volumetric excess of solution based on the pore volume of the carbon. The resulting slurry was filtered on a Büchner funnel under suction. To remove residual liquid on the surface of the carbon, the product was sandwiched between sheets of filter paper and gently squeezed. The solid product was calcined in air in a muffle furnace. A heating ramp of 15 °C/min was used, the final calcination temperature being 500 °C unless otherwise indicated (it should be noted that use of a faster heating ramp, e.g., 20 °C/min, was found to result in violent combustion of the template in some cases). Platinum-loaded ceria samples were prepared by means of incipient wetness impregnation, using tetraammine platinum(II) nitrate [8].

Characterization

The surface area, pore volume and average pore radius of the carbon templates were determined by BET and DFT methods using ASAP 2010 and ASAP 2020 porosimetry systems. Those of the ceria products were determined using a Micromeritics Tri-Star system. N_2 at –196 °C was the sorbate. In all cases samples were outgassed overnight at 160 °C prior to the measurements. Powder X-ray diffraction (XRD) measurements were performed on a Phillips X'Pert diffractomer using Cu Kα radiation (λ = 1.5406 Å) and a step size of 0.02°. Peak simulation was performed using a standard fitting program [34]. Average crystallite sizes were calculated using Fourier Integral Breadth analysis. Calculations were based on the (111) line at ca. 2θ = 29°, this being the most intense line in the XRD patterns. Thermogravimetric analyses were performed on a Netzsch

Table 1 Physical characteristics of carbon templates

Carbon template	Activation temperature (°C)	Activation time (h)	BET surface area (m^2 g^{-1})	Pore volume (cm^3 g^{-1})	Average pore diameter (nm)	Pore size distribution		
						Micro (%)	Meso (%)	Macro (%)
Darco KB-B	–	–	1550	1.222	4.04	22.5	71	6.5
Anshan P-400[a]	–	–	60.5	0.023	1.87	100	0	0
ACF-718	800	1	718	0.235	<2.0	100	0	0
ACF-1258	800	3	1258	0.491	1.89	87.9	12.1	0
ACF-1368	900	1	1368	0.511	1.76	81	7	12
ACF-1552	825	3	1552	0.635	1.96	90	10	0
ACF-2009	850	3	2009	0.932	2.15	60	40	0

[a] Carbon fibers prior to activation

STA 449C thermogravimetric analyzer. Samples were analyzed in an atmosphere of flowing He (100 cm^3/min) using a heating rate of 20 °C/min to 1,000 °C. Mass spectra were acquired from the gas exiting the TG furnace in multiple ion detection mode. High-resolution transmission electron microscopy (HRTEM) measurements were carried out with a JEOL 2010 FasTEM field emission electron microscope operated at an accelerating voltage of 200 kV, equipped with a field emission gun, Oxford EDS detector with Emispec EsVision computer control system, a Gatan CCD multiscan camera, Gatan image filter (GIF) and Gatan Digiscan II. The electron beam has a point-to-point resolution of 0.3 nm. The sample material was lightly dusted onto 200-mesh Cu grids coated with lacy carbon. Scanning electron microscopy (SEM) was performed using a Hitachi S-2700 instrument equipped with a LaB_6 electron gun and a PGT EDS analyzer with thin window detector.

Diffuse reflectance infrared Fourier transform spectroscopy (DRIFTS) measurements were performed using a Nicolet Nexus 870 instrument, equipped with a DTGS-TEC detector. An in situ chamber fitted with ZnSe windows was employed for CO adsorption measurements. Scans were taken at a resolution of 4 to give a data spacing of 1.928 cm^{-1}. About 128 scans were taken to improve the signal to noise ratio. The sample amount was 33 mg. Feed gases (UHP) were controlled with Brooks 5850 series E mass flow controllers. An iron carbonyl trap, consisting of lead oxide on alumina (i.e., Calsicat), was placed on the CO gas line. Hydrogen reduction was first carried out using a flow of 100 cm^3/min, and the catalyst was purged in flowing nitrogen (135 cm^3/min). During CO adsorption, the gas flows were maintained at 3.75 cm^3/min CO and 135 cm^3/min N_2.

Results and discussion

Template characteristics

Two types of carbon template were examined in this work: activated carbon fibers and an activated carbon powder, Darco KB-B. Physical characteristics of the templates are summarized in Table 1. Darco KB-B is a commercial carbon powder which according to nitrogen physisorption data possesses high mesoporosity, and also contains both micropores and macropores. In contrast, porosity in the activated carbon fibers (ACFs) used in this study is associated mainly (or even wholly) with micropores. In general, higher activation temperatures and longer treatment times afforded fibers with increased surface area, mesoporosity and total porosity. The use of high temperatures in particular was found to be beneficial for the introduction of mesoporosity. Thus steam treatment of carbon fibers at 800 °C for 1 h afforded a product containing only micropores (ACF-718), whereas after activation at 900 °C for 1 h fibers containing small amounts of both mesopores and macropores were obtained (ACF-1368). Similarly, comparison of ACF-1552 and ACF-2009 reveals that increasing the activation temperature from 825 to 850 °C results in a significant increase in the porosity present corresponding to mesopores (10% versus 40% of total porosity, respectively). While these treatments are successful in introducing porosity into the fibers, their bulk morphology is largely unaffected. Thus SEM images of ACF-1368 (Fig. 1) reveal a typical carbon fiber morphology, with little evidence for deformed or severely etched fibers.

Cerium oxide preparation

For cerium oxide preparation, the carbon templates were loaded with cerium nitrate using a wet impregnation method. Subsequently, the templates were gasified by heating in air at 500 °C for 2 h. Using these conditions complete removal of the template was achieved. Thermogravimetric analysis indicated that in the absence of the cerium salt, temperatures in excess of 600 °C were required for complete combustion of the Darco KB-B or ACF templates; for the Darco KB-B material, this temperature was determined to be 630 °C. From this it follows that the ceria product significantly lowers the combustion temperature of the template. This is not unexpected, given that ceria is used both as a fuel additive to catalyze the combustion

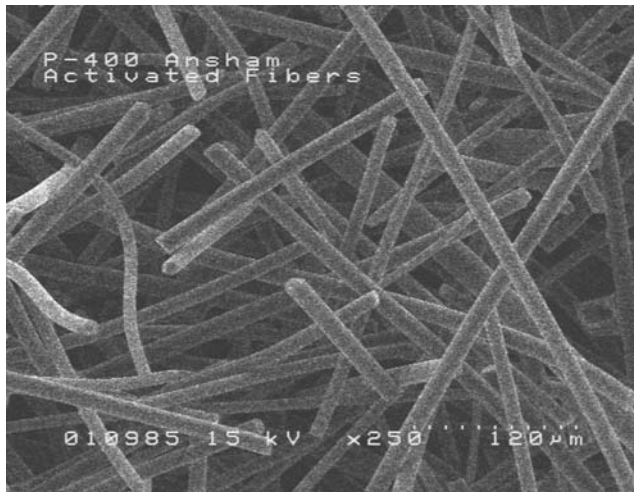

Fig. 1 SEM image of ACF-1368

of diesel soot on uncatalyzed diesel particulate filters, and as a washcoat component of catalyzed particulate filters [35]. In the case of the Darco KB-B carbon, use of this procedure afforded a ceria product with a surface area of 125 m^2/g (Table 2). XRD showed the product to be crystalline (Fig. 2), an average crystallite size of 6.5 nm being calculated from line broadening of the (111) peak. In comparison, calcination of cerium nitrate in the absence of the template afforded ceria with a surface area of 20 m^2/g when calcined under the same conditions.

Variation of the concentration of the cerium nitrate solution used for the impregnation within the range 2.9–4.0 M was found to have no perceivable effect on the surface area or pore volume of the ceria formed. However, in line with previous findings for a variety of other metal oxides [22], the use of more dilute solutions (e.g., 0.5 M) was found to adversely affect the surface area of the ceria product. The calcination protocol was also indicated to be of importance. An optimized protocol, based on thermogravimetric data (vide infra), consisted of first calcining the impregnated Darco KB-B carbon at 250 °C, during which exothermic decomposition of the cerium nitrate occurred, accompanied by carbon oxidation by released NO_2. This step was followed by a final calcination at 450 °C, to facilitate ceria-catalyzed combustion of the residual carbon by O_2. In this manner the ceria product was exposed to lower temperatures as compared to ramping directly to 500 °C. The resulting ceria possessed high surface area (148.3 m^2/g, see Table 2), while the residual carbon content of 0.17 wt% was comparable with that of ceria obtained after calcination at 500 °C (typically 0.1–0.3 wt%). The carbon content of these materials can be attributed in large part to the presence of surface carbonates: in control experiments, precipitated cerium oxide, after calcination and subsequent exposure to air for several days, typically showed a carbon content of 0.1–0.2 wt%. IR spectra of these materials were found to contain weak bands at 1,630 and 1,506 cm^{-1} which may be assigned to hydrogen carbonate and monodentate carbonate species, respectively [36].

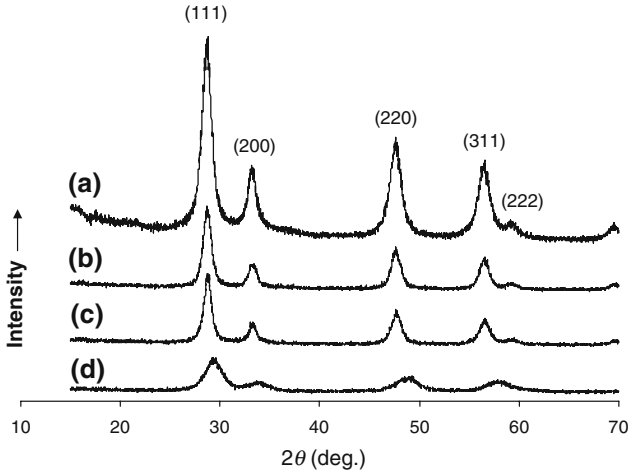

Fig. 2 X-ray diffraction patterns of (**a**) CeO_2 prepared without template, (**b**) CeO_2 templated from ACF-718, (**c**) CeO_2 templated from Darco KB-B, and (**d**) $Ce_{0.5}Zr_{0.5}O_2$ templated from Darco KB-B

In addition to ceria, the preparation of ceria-zirconia was examined. Mixed oxides of this type are of particular interest given their superior oxygen storage properties relative to ceria, as well as improved thermal stability with respect to sintering [37]. Impregnation of Darco KB-B with an aqueous solution containing $Ce(NO_3)_3$ and $ZrO(NO_3)_2$ (0.7 M in each), followed by the two-step calcination procedure described above, afforded $Ce_{0.5}Z_{0.5}O_2$ with a surface area of 148 m^2/g (Table 2) and residual carbon content of <0.2 wt%. XRD showed the product to be crystalline (Fig. 2) with an approximate average crystallite size of 3.6 nm. In agreement with the literature [37], relative

Table 2 Physical characteristics of ceria and ceria-zirconia prepared using carbon templates

Carbon template	Template BET SA (m^2 g^{-1})	Calcination temperature (°C)	Product	BET SA (m^2 g^{-1})	Pore volume (cm^3 g^{-1})	Pore diameter (nm)
–	–	500	CeO_2	20.0	0.057	11.5
Darco KB-B	1550	500	CeO_2	124.5	0.242	7.8
Darco KB-B	1550	450[a]	CeO_2	148.3	0.289	7.8
Darco KB-B	1550	450[a]	CeO_2–ZrO_2[b]	148.0	0.23	5.7
ACF-718	718	500	CeO_2	3.2	0.013	17.0
ACF-1258	1258	500	CeO_2	21.0	0.106	20.2
ACF-1368	1368	500	CeO_2	59.4	0.312	21.0
ACF-1552	1552	500	CeO_2	26.7	0.081	12.2
ACF-2009	2009	500	CeO_2	37.2	0.278	30.0

[a] Calcined in two stages (250 °C/1 h, 450 °C/1 h)

[b] Ce/Zr = 1.0

to ceria the (111) diffraction peak is shifted from 28.8° to 29.2° for the mixed oxide, consistent with a change in the lattice parameter and indicative of the presence of a solid solution.

Thermogravimetric analysis performed on Darco KB-B carbon impregnated with cerium nitrate revealed that oxidation of the carbon template commences simultaneously with decomposition of the cerium salt, being facilitated by the release of NO_2 from the Ce compound. Gasification of the template is complete by 500 °C. The role of NO_2 in template oxidation was substantiated by thermogravimetric analysis performed in flowing He (Fig. 3). During heating to 1,000 °C, eight distinct weight loss regions can be identified based on the differential of the weight loss curve (DTG). These weight losses are given in Table 3. The first weight loss region (up to 113 °C) can be attributed to loss of physisorbed water. The second region (113–178 °C) corresponds to the largest loss in sample weight. In this region an exothermic DTA maximum (531 J/g) is observed, and NO, NO_2, and CO_2 are simultaneously evolved with H_2O. Weight loss regions three and four similarly contain small DTA maxima and exhibit NO_2, CO_2 and H_2O evolution. Above 300 °C small amounts of CO_2, NO, NO_2 and H_2O continue to be released. The observation that

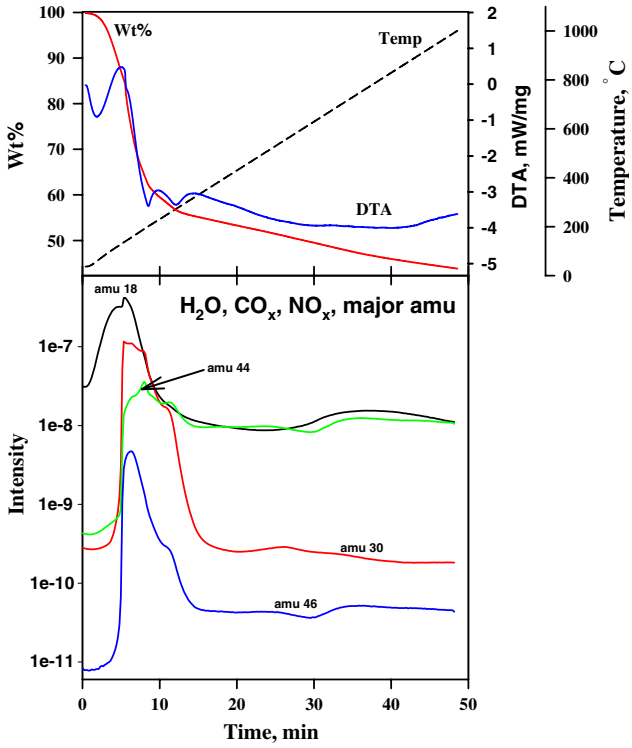

Fig. 3 Thermogravimetric analysis in flowing He of Darco KB-B activated carbon impregnated with cerium nitrate

NO_x (primarily NO_2), and CO_2 are simultaneously evolved during the exothermic DTA maximum observed at 140 °C is consistent with decomposition of the cerium nitrate and concomitant oxidation of the carbon template by the released NO_2.

In contrast to the results obtained with Darco KB-B carbon, ceria preparation using activated carbon fibers as template afforded a product possessing low to moderate surface area (3–59 m^2/g), with a gross morphology resembling that of the fiber template. In all cases a calcination temperature of 500 °C was required to effect combustion of the template, the residual carbon contents of the products falling in the range 0.2–0.4 wt%. The lower surface areas of the ceria fibers reflect the largely microporous nature of the ACFs; evidently the Ce nitrate solution is largely unable to penetrate their micropores. Consequently, mesoporosity and macroporosity appear to be the main determinants with respect to the surface area of the ceria product. ACF-1368 provided the highest surface area product, presumably as a consequence of its combination of mesoporosity and macroporosity, while the surface areas of the other cerias followed the order of mesopore volume, and surface area, of the ACF templates (ACF-2009 > ACF-1552 > ACF-1258 > ACF-718).

Figure 4 shows the nitrogen adsorption isotherms of ceria templated from Darco KB-B and ACF-2009. The corresponding pore size distribution plots are given in Fig. 5. For the Darco-templated ceria the isotherm displays Type II (multi-layer) adsorption behavior over most of the reduced pressure range, with type H3 hysteresis (IUPAC classification). The type H3 loop, which does not exhibit any limiting adsorption at high P/P_0, is characteristic of non-rigid aggregates of plate-like particles giving rise to slit-shaped pores [38]. These observations are also indicative of a pore size distribution extending into the macropore range. In the case of ceria prepared using the ACF-2009 template, the nitrogen adsorption isotherm approximates to a type IV isotherm, characteristic of a mesoporous material. The hysteresis loop is small and possesses features reminiscent of both the H3 and H1 type. The fact that adsorption appears to limiting at high P/P_0 suggests that the latter classification is a more valid description. Type H1 hysteresis is usually associated with solids consisting of nearly cylindrical channels or agglomerates or compacts of near uniform spheres.

Electron microscopy

Further insights into the textural and morphological properties of the ceria products were provided by

Table 3 Thermogravimetric analysis in He of Darco KB-B impregnated with cerium nitrate

Start temperature (°C)	37	113	178	242	310	756	Total
End temperature (°C)	113	178	242	310	756	1000	
% Weight loss	8.88	24.06	8.32	3.23	8.45	3.10	56.04

transmission electron microscopy (TEM). For ceria templated from Darco KB-B activated carbon, TEM reveals the presence of a polycrystalline phase consisting of individual ceria crystals, all of which occur within a narrow size range of ~5–10 nm. The majority of the ceria crystals are clustered in aggregates with dimensions of typically 200–400 nm (Fig. 6). Specific preferential crystal orientations are not observed, the ceria crystals being randomly oriented in a 3D array. In the denser areas of the agglomerates particle stacking is apparent (up to several layers), while in the extremely thin areas at the outer region of the agglomerates ceria crystals occur only in one layer. These thin areas allow the interfacial regions between individual crystals to be observed, and it is apparent that crystals are typically surrounded by voids. These voids completely engulf the individual ceria particles, such that they are well separated. Many of the primary particles in the aggregates appear to possess straight edges, implying the presence of flat crystal faces. Consistent with the results of powder XRD measurements, a particle diameter of 5–10 nm is indicated.

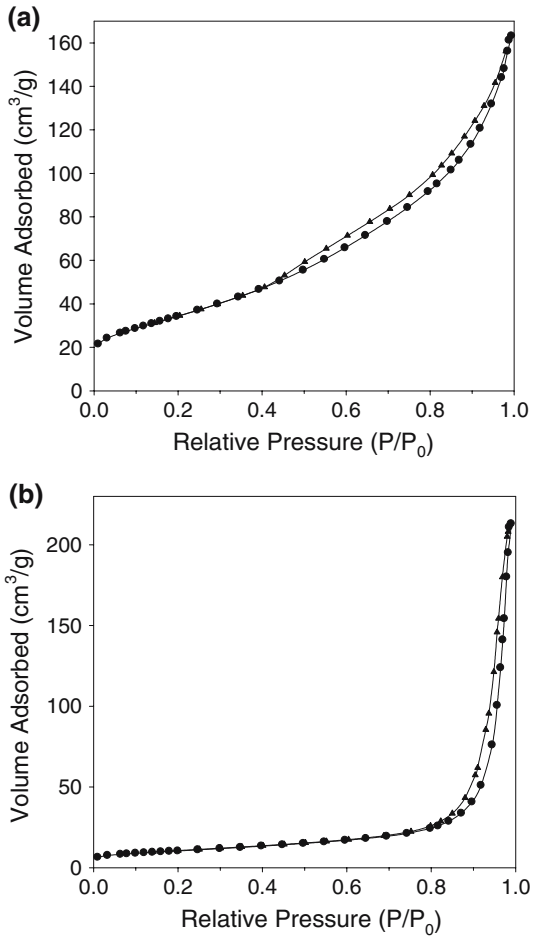

Fig. 4 N_2 adsorption/desorption isotherms for ceria templated from (**a**) Darco KB-B and (**b**) ACF-2009

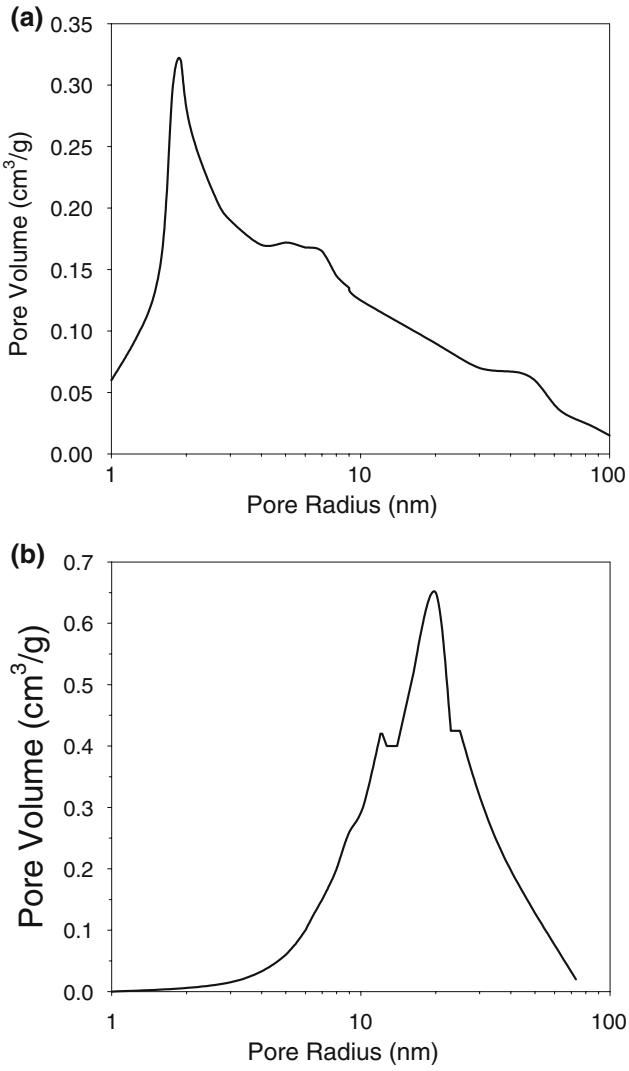

Fig. 5 Pore-size distribution plots derived from N_2 adsorption isotherms for ceria templated from (**a**) Darco KB-B and (**b**) ACF-2009

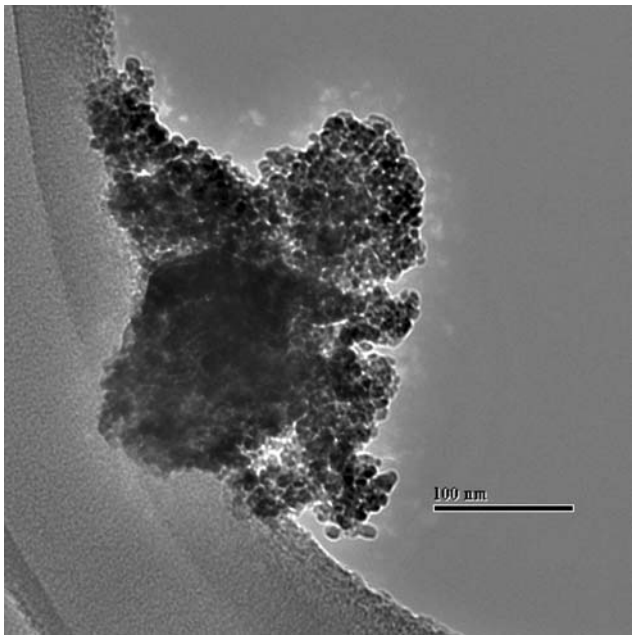

Fig. 6 TEM image of ceria aggregate templated from Darco KB-B activated carbon

In the case of ceria templated from carbon fibers, SEM (Fig. 7) and low-resolution TEM (Fig. 8) images indicate a fibrous or needle-like morphology for the ceria product. As shown in Fig. 7, ceria prepared from ACF-718 consists of roughly spherical ~150–250 μm diameter aggregates that are composed of an interlocked network of needle-like structures. The formation of these structures appears to reflect the rather

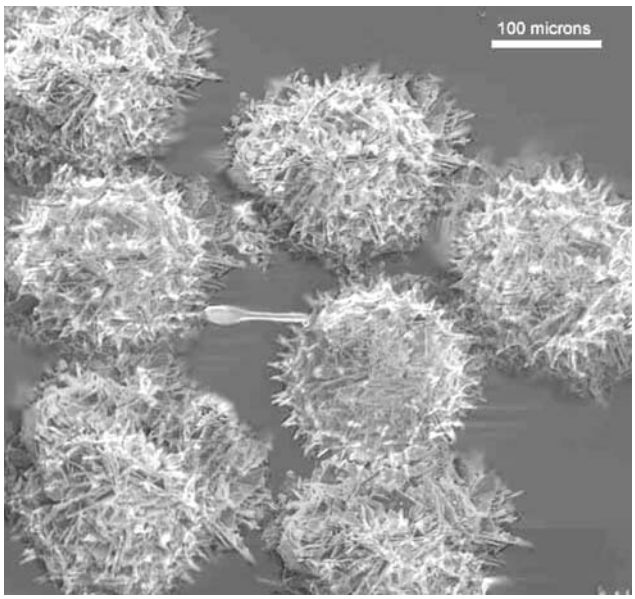

Fig. 7 SEM image of ceria fiber aggregates templated from ACF-718

hydrophobic nature of the ACF-718 fibers and their resulting tendency to form aggregates when suspended in water (and hence during wet impregnation with cerium nitrate). Increasing the severity of the fiber activation resulted in reduced hydrophobicity (due to the greater degree of functionalization with surface oxygen groups [39]), with the consequence that the other ACF templates showed little or no tendency to form such aggregates.

While higher resolution SEM images (not shown) indicate a certain surface roughness and hole or cavity formation along the exterior of the cerium oxide needles, TEM results provide added information concerning their porosity. The fact that TEM in general is more of a 2D analytical method suggests that pores may be difficult to detect. However, for the cerium oxide needles the transparency of the areas where large pores formed within the needles is much greater compared with the bulk of the structures, such that the pores appear as light-colored areas (Fig. 8a, b). When adjusting the focus it is possible to image other layers within the needle and reveal pores at a different depth level. An example of this is illustrated in Fig. 8b. This image reveals the presence of macropores with diameters of ca. 30–100 nm at the needle surface, which appear to have formed via the action of escaping gases during gasification of the carbon template. Based on the nitrogen physisorption data, these macropores evidently do not contribute significant porosity to the ceria. At higher resolution the presence of smaller pores (ca. 10 nm) is apparent; these may also result from the gasification process or derive from crystallization of ceria around micropore or small mesopore openings in the template. Ridge-like structures are also observed at the surface of the needle depicted in Fig. 8. These are most likely diffraction artifacts resulting from thickness variations along the fiber axis, since these features are lost at high-resolution imaging of individual ceria crystallites within the vicinity of the ridges.

Based on the foregoing SEM and TEM data, it is apparent that cerium nitrate is deposited principally on the external surface of the carbon fiber, subsequent gasification of the template and ceria crystallite growth giving rise to the observed morphology. This suggests that the ceria fibers should be hollow; however, this could not be ascertained definitively from the TEM images due to the dense packing of the ceria crystallites on the fiber surface. The presence of the macropores, noted above (Fig. 8), corresponds to areas which are a much lighter (brighter) shade of gray than the surrounding area; for TEM images this typically suggests that the area of interest is thinner and, hence, more

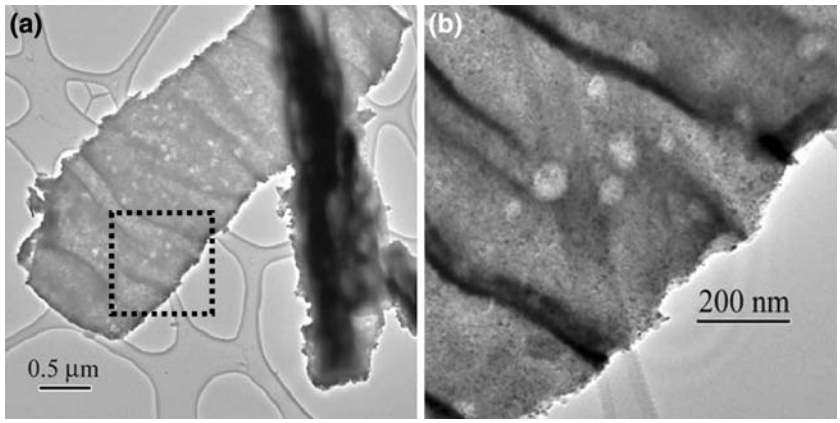

Fig. 8 (**a**) TEM image of ceria fibers templated from ACF-718 and (**b**) detail (*boxed region*) showing macropores

transparent compared with the darker areas surrounding the pores. High magnification images show, however, the presence of ceria crystallites at the base of the pores, which in turn suggests (a) the fibers are hollow and the base represents the opposite fiber wall or, (b) the pores are rather deep in nature. Future studies employing 3D-nanotomography should establish with certainty whether the fibers are indeed hollow.

Higher resolution TEM images (Fig. 9a) show that the needles are actually aggregates of crystallites which are similar in morphology and size to those observed for the Darco KB-B templated ceria, albeit rather more crystalline in appearance. Most of the crystallites imaged possess straight edges, and, as for the Darco KB-B templated ceria, specific preferential crystal orientations are not observed. The (111) surface is the most stable surface for CeO_2. In our HRTEM work we observed that the majority of CeO_2 particles show the (111) surfaces in corresponding lattice images, followed, in terms of abundance, by the (200) and (220) surfaces. While the ceria particles, which have a narrow size range of ~4–8 nm, are arranged in a dense packing, it is nevertheless apparent that void spaces are present between the individual crystals, especially in very thin regions where only a few crystallites are stacked on one another (Fig. 9). The void space between individual crystallites results from the size, shape and orientation mismatch of individual crystallites, and implies a degree of pore connectivity in the sample and associated mesoporosity.

The corresponding electron diffraction pattern in Fig. 9b shows the polycrystalline nature of the ceria agglomerates within the fibrous structure depicted in Fig. 9a. The area selected for the electron diffraction pattern includes a large number of crystallites and the corresponding pattern is not reminiscent of the symmetry of one crystallite. The specific ring spacing in the electron diffraction pattern corresponds to the cubic lattice, further suggesting that individual ceria nanoparticles are near single crystals. However, the multiple ring formation also reveals that the ceria crystallites are oriented rather randomly and that individual crystals do not have a preferred orientation along the fiber axis. The calculated lattice parameter of 5.44 Å

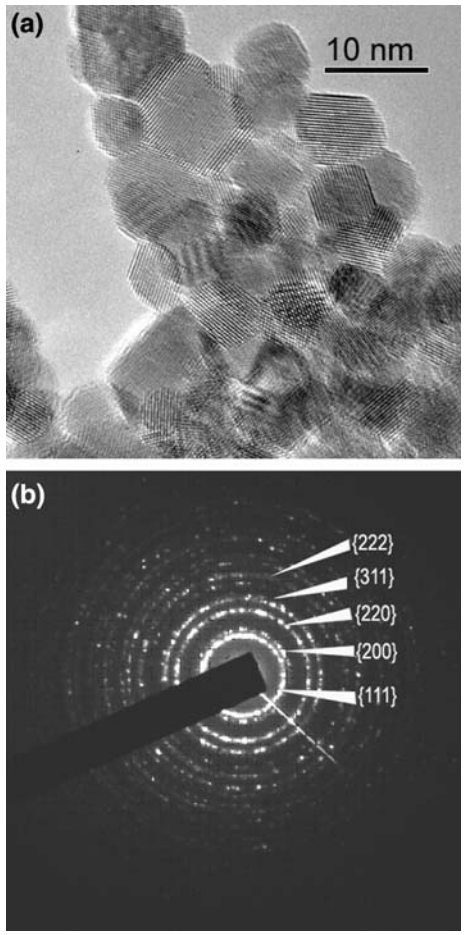

Fig. 9 (**a**) High-resolution TEM image of ACF-718 and (**b**) corresponding electron diffraction pattern

compares with the literature value of 5.41 Å for well-crystallized CeO_2. The small lattice expansion observed for the CeO_2 nanocrystallites is in accordance with nanosize-induced strain effects reported by Zhang et al. [40].

For the fibers prepared from ACF-1552, TEM images reveal the majority of the fibers to be similar in appearance to those observed for ACF-718 (Fig. 8), with dense packing of the ceria crystallites and little evidence of porosity (in keeping with the low pore volume determined by nitrogen physisorption). The presence of smaller fibers was also observed (Fig. 10). In this case the fiber is composed of ceria crystallites which are aligned perpendicularly to the main fiber axis. Given the small diameter of the fiber (35–40 nm), this structure likely corresponds to part of a larger ceria fiber which has become detached. Crystallites at the edges of the fibers are again found to possess a platelet morphology, with a crystallite size in the range 5–10 nm being indicated. As for ceria templated from ACF-718, high resolution micrographs reveal evidence of crystallites with well defined edges and strong faceting.

Detection of surface defect sites

CO adsorption on hydrogen-reduced Pt/ceria catalysts has been used to characterize reduced defect centers on the surface of ceria [41], which are important in heterogeneous catalysis. Upon reduction in hydrogen, Type II bridging OH groups are generated on the surface of ceria [42, 43], most likely the result of spillover of dissociated atomic hydrogen from Pt to the ceria surface [4]. The Type II bridging OH groups are associated with cerium atoms in the Ce^{3+} oxidation state after the surface shell reduction process. Upon adsorption of CO, the bridging OH groups react with CO to generate surface formate species [4, 44, 45]. Infrared spectroscopy is an important technique for characterizing these reduced centers, as bands characteristic of the formate species are readily observed. In order to confirm the formation of such sites on the carbon-templated ceria, a sample of the Darco KB-B templated material (surface area 125 m^2/g) was loaded with Pt (1 wt%) for comparison with a reference sample. The latter comprised 1 wt% Pt loaded onto a ceria of identical surface area (125 m^2/g) synthesized by the urea precipitation-gelation method [9]. Characterization data for the reference has been reported previously [4]. According to TEM data Pt in the reference is highly dispersed, Pt particle sizes falling in the range 0.5–1.5 nm. For the sample prepared using the carbon templated cerium oxide, IR data (see below) suggest a similarly high Pt dispersion.

Upon reduction of both 1% Pt/ceria samples at 250 °C in flowing hydrogen, chemisorbed CO_2 is removed as evidenced by the disappearance of weak bands corresponding to hydrogen carbonate and monodentate carbonate species. As shown in Fig. 11, subsequent adsorption of CO results in a sharp decrease in the band at 3,650 cm^{-1} characteristic of Type II bridging OH groups, and the evolution of bands for the formates, including OCO asymmetric and symmetric modes at ~1,580 and ~1,300 cm^{-1}, respectively, and accompanying bands for C–H stretching (2,845 and 2,950 cm^{-1}). An additional broad band occurring at ~2,060–1,870 cm^{-1} corresponds to CO adsorbed on Pt; this asymmetric band includes a number of contributions from linearly adsorbed CO (~2,060–2,000 cm^{-1}) and a band that is tentatively assigned to bridge-bonded CO at ~1,980–1,870 cm^{-1}. For the two samples the combined Pt-CO band is of approximately equal intensity, indicating that the Pt dispersions are similar. In addition, as noted previously [4], the intensities of surface formate bands provides some indication of the density of reduced centers on

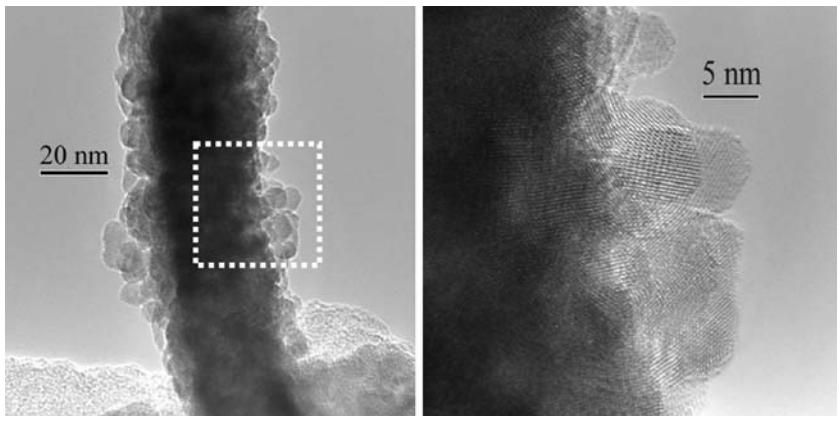

Fig. 10 TEM images of ceria fiber templated from ACF-1552 and detail (*boxed region*) showing alignment of ceria platelets

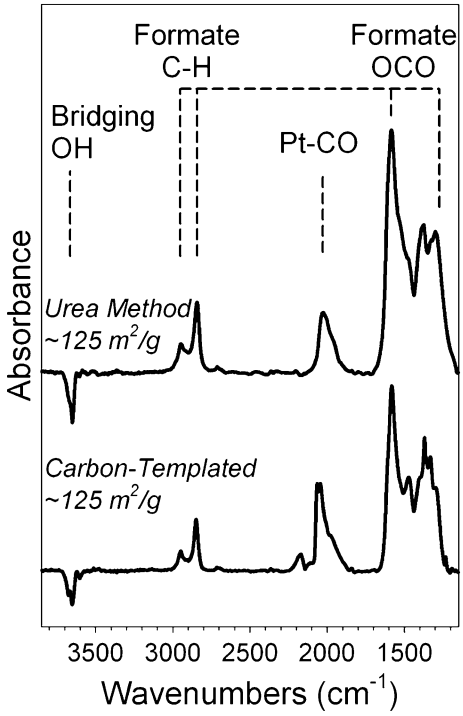

Fig. 11 In situ DRIFTS spectra of reduced 1% Pt/ceria samples exposed to CO at 250 °C

the surface of the catalyst. For both samples the observed formate bands were intense, the band intensities for the 1% Pt/ceria sample produced from the carbon-templating method appearing slightly less than, but of the same order of magnitude as, those obtained for the sample prepared using the precipitated ceria. These observations suggest that for both ceria supports a high density of active sites is obtained on the surface of the Pt-loaded materials.

Conclusions

Carbon templating represents a convenient method for the preparation of high surface area cerium oxide and cerium–zirconium mixed oxide. The use of an activated carbon with high mesoporosity as template (Darco KB-B) afforded crystalline ceria and ceria-zirconia with surface areas as high as 148 m^2/g. This figure compares favorably with results typically obtained with simple solution methods (e.g., the citrate route), while the carbon templating approach avoids the drawbacks associated with other solution methods such as reverse microemulsion synthesis (large volumes of organic solvents) and hydrothermal synthesis (use of expensive surfactant as template). Carbon templating using activated carbon fibers (ACFs) was found to provide a simple route to fibrous cerium oxide. Ceria fiber formation appears to proceed via crystallite growth on the outer surface of the ACF, followed by gasification of the ACF. For Darco-templated ceria, irregularly shaped aggregates were obtained, derived from crystallite growth in the template pores.

Acknowledgement The authors wish to thank Mr. G. Thomas for performing the XRD measurements.

References

1. Kaspar J, Fornasiero P, Graziani M (1990) Catal Today 50:285
2. Yoo J, Bhattacharyya A, Radlowski C, Karch J (1992) Appl Catal B: Environ 1:169
3. Trovarelli A, De Leitenburg C, Boaro M, Dolcetti G (1999) Catal Today 50:353
4. Jacobs G, Graham UM, Chenu E, Patterson PM, Dozier A, Davis BH (2005) J Catal 229:499
5. Liu Y, Fu Q, Flytzani-Stephanopoulos M (2004) Catal Today 93–95:241
6. Philipp S, Drochner A, Kunert J, Vogel H, Theis J, Lox ES (2004) Topic Catal 30/31:235
7. Wang F-Y, Chen S, Cheng S (2004) Electrochem Commun 6:743
8. Jacobs G, Williams L, Graham UM, Thomas GA, Sparks DE, Davis BH (2003) Appl Catal A: Gen 252:107
9. Liu Y, Fu Q, Flytzani-Stephanopoulos M (2000) Appl Catal B: Environ 27:179
10. Bugayeva N (2005) In: Lu SW, Hahn H, Weissmuller J, Gole JL (eds) Mater Res Soc Symp Proc 876E, R8.46
11. Masiu T, Fujiwara K, Machida K, Adachi G, Sakata T, Mori T (1997) Chem Mater 9:2197
12. Alifanti M, Baps B, Blangenois N, Naud J, Grange P, Delmon B (2003) Chem Mater 15:395
13. Nakane S, Tachi T, Yoshinaka M, Hirota K, Yamaguchi O (1997) J Am Ceram Soc 80:3221
14. Overbury SH, Huntley DR, Mullins DR, Glavee GN (1998) Catal Lett 51:133
15. Lyons DM, Ryan KM, Morris MA (2002) J Mater Chem 12:1207
16. Thundathil MA, Lai W, Noailles L, Dunn BS, Haile SM (2004) J Am Ceram Soc 87:1442
17. Laberty-Robert C, Long JW, Lucas EM, Pettigrew KA, Stroud RM, Doescher MS, Rolison DR (2006) Chem Mater 18:50
18. Yang H, Zhao D (2005) J Mater Chem 15:1217
19. Kang M, Kim D, Yi SH, Han JU, Yie JE, Kim JM (2004) Catal Today 93–95:695
20. Schwickardi M, Johann T, Schmidt W, Busch O, Schüth F (2002) Stud Surf Sci Catal 143:93
21. He J, Kunitake T, Watanabe T (2005) Chem Commun, 795
22. Schwickardi M, Johann T, Schmidt W, Schüth F (2002) Chem Mater 14:3913
23. Ozawa M, Kimura M (1990) J Mater Sci Lett 9:446
24. Wakayama H, Itahara H, Tatsuda N, Inagaki S, Fukushima Y (2001) Chem Mater 13:2392
25. Yue Z, Pripusich-Sienkiewicz KE, Economy J (2003) Preprints of extended abstracts, Division of Environmental Chemistry, ACS National Meeting, NY, 43(2):432
26. Kim HJ, Nam KH, Shul YG (2003) Mater Sci Forum 439:271

27. Li W-C, Lu A-H, Weidenthaler C, Schüth F (2004) Chem Mater 16:5676
28. Dong A, Ren N, Tang Y, Wang Y, Zhang Y, Hua W, Gao Z (2003) J Am Chem Soc 125:4976
29. Kim JY, Yoon SB, Yu J–S (2003) Chem Commun, 790
30. Kim JM, Kang M, Hwan S, Yie JE, Joo SH, Ryoo R (2003) Stud Surf Sci Catal 146:53
31. Ajayan PM, Stephan O, Redlich Ph, Colliex C (1995) Nature 375:564
32. Satishkumar BC, Govindaraj A, Nath M, Rao CNR (2000) J Mater Chem 10:2115
33. Crocker M, Graham U, Gonzalez R, Morris E, Jacobs G, Andrews R (2005) In: Lu SW, Hahn H, Weissmuller J, Gole JL (eds) Mater Res Soc Symp Proc 876E, R4.2
34. Krumm S. Winfit, version 1.2; http://www.geol.uni-erlangen.de
35. Summers JC, Van Houtte S, Psaras D (1996) Appl Catal B: Environ 10:139
36. Binet C, Daturi M, Lavalley J-C (1999) Catal Today 50:207
37. Hori CE, Permana H, Ng KYS, Brenner A, More K, Rahmoeller KM, Belton D (1998) Appl Catal B: Environ 16:105
38. Lowell S, Shields JE, Thomas MA, Thommes M (2004) Characterization of porous solids and powders: surface area, pore size and density. Kluwer Academic Publishers, Dordrecht, p 44
39. Boehm HP (1994) Carbon 32:759
40. Zhang F, Jin Q, Chan S-W (2004) J Appl Phys 95:4319
41. Lavalley J–C (1996) Catal Today 27:377
42. Binet C, Badri A, Lavalley J-C (1994) J Phys Chem 98:6392
43. Laachir A, Perrichon V, Badri A, Lamotte J, Catherine E, Lavalley J-C, El Fallah L, Le Normand F, Quemere E, Sauvion GN, Touret O (1983) J Chem Soc Faraday Trans 79:2219
44. Shido T, Iwasawa Y (1993) J Catal 141:71
45. Li C, Domen K, Maruya K–I, Onishi T (1990) J Catal 125:445